Pratibha Sharma, Matthew M. Wilkins, Henry P. Schriemer, Karin Hinzer, "Concentrating optical system optimization for 3- and 4-junction solar cells: impact of illumination profiles," J. Photon. Energy 7(1), 014501 (2017), doi: 10.1117/1.JPE.7.014501.

Concentrating optical system optimization for 3- and 4-junction solar cells: impact of illumination profiles

Pratibha Sharma*, Matthew M. Wilkins, Henry P. Schriemer, Karin Hinzer
University of Ottawa, SUNLAB, School of Electrical and Computer Engineering,
25 Templeton Street, Ottawa, ON, Canada, K1N6N5

Abstract. Optical component designs for concentrating photovoltaic systems with three different multijunction solar cells are optimized to yield maximum system efficiencies under standard test conditions, specifically uniform illumination. Optimization uses an integrated optoelectrical approach with ray tracing of the optical train to generate an irradiance profile for input to the cell's distributed circuit model. These cells, a three-junction lattice-matched (3JLM) solar cell, a three-junction lattice-mismatched inverted metamorphic (3JIMM) solar cell, and a four-junction lattice-matched (4JLM) solar cell, were individually designed for maximum efficiency at 1000X. The optical train introduces losses, modifies the spectrum, and produces a spatially nonuniform profile across the cell. We decouple spectral modification from spatial nonuniformity to separately determine their individual impacts on system efficiencies, finding the optimal set of optical design parameters for each case. Spectral modification yields modest loss penalties (from 1.0 to 1.6%, relative to the MJSC), but the impact of nonuniformity is more significant and cell dependent, with relative loss penalties of 1.1, 3.8 and 2.3%, for 3JLM, 3JIMM and 4JLM, respectively. While spectral modification does not significantly impact design parameters, spatial nonuniformity does, with absolute losses of 1 and 3.4% if 3JIMM and 4JLM cells are used in a 3JLM optimized system.

Keywords: concentrated photovoltaic, distributed circuit model, nonuniform illumination, four-junction solar cell, three-junction solar cell, spectral variations.

* E-mail: psharm2@uottawa.ca

1. Introduction

Multijunction solar cells (MJSCs) have demonstrated record efficiencies under concentration [1]. The rapid rise in MJSC efficiencies has led to a strong interest in concentrated photovoltaic (CPV) technologies. However, even though MJSC efficiencies are high, system losses markedly reduce module efficiencies [2]. While losses in the optical train play a major role, the nonuniform illumination profiles generated by concentrating elements can lead to ohmic losses that reduce the fill factor and hence decrease CPV system efficiency [3]. Figure 1 shows an illustration of spatial profiles for a uniformly illuminated and a nonuniformly illuminated solar cell. The nonuniformly

illuminated cell may see irradiance peaks which are several times larger than a uniformly illuminated cell.

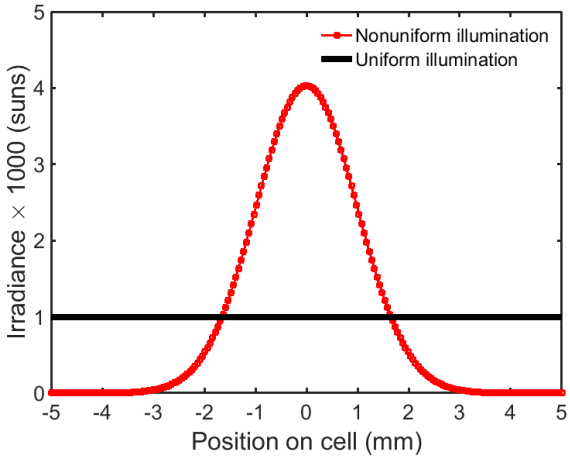

Fig. 1 Uniform and nonuniform Gaussian irradiance profiles on a solar cell. 1 sun is defined as 1000 W/m^2.

Nonuniform effects have been studied using experimental [4, 5] and modeling approaches [6, 7, 8]. Among the latter, it has been found that optimizing grid spacing can partially compensate for losses due to nonuniform illumination [8]. Additionally, spectrally modified spatial profiles in lens-based CPV systems can also reduce system efficiencies. Focal point variation with wavelength causes a spectral mismatch between the subcells, driving current production away from the nominal design point [9-12]. Since the impact of spatial and spectral nonuniformities depends on the MJSC design, the CPV system optical train has to be optimized for the specific cell designs.

In this paper, we optimize a well-understood optical system to understand the effect of spectral and spatial variations on three different cell designs: a lattice-matched three-junction solar cell; a lattice-mismatched inverted-metamorphic three-junction solar cell; and a lattice-matched four-junction solar cell. Section 2.1 discusses the results of numerical modeling for the three designs. Subcell current-voltage (I-V) curves and external quantum efficiencies have been obtained using drift-diffusion simulations. Parametrized distributed circuit models, detailed in section 2.2, are created using SPICE for each design using individual subcell I-V characteristicts. Details on the concentrating optics are presented in section 2.3 along with the definitions for the system optimization parameters.
Results are presented in section 3 along with a detailed comparative analysis. Design sensitivities to system parameters and optical variation are discussed. For each MJSC, we perform an opto-electrical CPV system simulation, employing ray tracing of the optical train to generate an irradiance profile for input to the MJSC's distributed circuit model. To focus on the spectral nonuniformity, we use a one-dimensional distributed circuit model with the intensity distribution input as a spatial average. Finally, the effects of spatial nonuniformity and spectrally-varying spatial profiles are both considered within a two-dimensional distributed circuit model. Multiparameter optimization of critical optical system dimensions is performed to achieve the maximum system efficiency for each MJSC design.

2. CPV system modeling and simulation

Distributed circuit models of MJSCs have been used to assess cell performance under concentration [13, 14], to determine optimal grid profiles [8], to understand tunnel junction limitations under concentration [15], and to explore spatial and spectral nonuniform illumination effects [16]. In order to determine the two-diode equivalent circuit parameters needed as inputs to the distributed circuit model [17], MJSC structures are simulated and optimized for the AM1.5D spectrum using Sentaurus Device [18], a commercially-available, drift-diffusion-based simulator. The simulations are performed using a linear grid with 5% grid-line shading on a 1 cm^2 cell area. Details on the set-up of the drift-diffusion simulations can be obtained elsewhere [19, 20].

2.1. MJSC designs

The first design is a typical lattice-matched three-junction cell (3JLM) with series-connected subcells composed of GaInP, InGaAs and Ge layers on a Ge substrate similar to [8]. Under 1 sun, the top two subcells are current matched at 13.6 mA/cm^2 while the bottom subcell overproduces at 22.5 mA/cm^2. The second design, a lattice-mismatched three-junction solar cell (3JIMM), has an inverted metamorphic configuration with a GaInP top layer, an InGaAs (1.4 eV) middle layer, and an InGaAs (1 eV) bottom layer [21]. At 1 sun, the top subcell and middle subcell are current-matched at 14.1mA/cm^2 while the short-circuit current density for the bottom subcell is 14.3 mA/cm^2. The third design, a four-junction, lattice-matched (4JLM) structure, is composed of GaInP, AlGaAs, and dilute nitride material on a doped Ge substrate. At 1 sun, the top and bottom subcells are almost current matched at 12.9 mA/cm^2. The second subcell (AlGaAs) slightly underproduces at 12.7 mA/cm^2 while the dilute nitride subcell overproduces at 13.3 mA/cm^2. Current overproduction in the dilute nitride subcell is required in order to compensate for its poor fill-factor [22, 23]. All the three designs have been designed with low-resistance tunnel junctions [24] and the anti-reflection coatings have been separately optimized for each design. The layers for each design have been separately optimized for maximum efficiency under uniform illumination. In the 4JLM design, since it is more important to collect maximum UV, a thinner window has been used to minimize absorption in the window.

The parameters used for circuit simulation are provided in the Appendix along with the detailed layer structures for each design. The external quantum efficiencies (EQEs) of the three designs are shown in Fig. 2. Solar cell EQEs are less than 1 due to optical transmission and reflection losses. The EQEs of the 3JLM design and 3JIMM design are simulated up to a maximum wavelength of 1800 nm while the 4JLM design simulation extends until 2000 nm. The third and fourth subcells in the four-junction structure (Fig. 2(c)) have reduced EQEs due to photon sharing between them. It can be seen that optical interference effects from the multiple layers above the lower subcells cause oscillations in the EQE, specifically in the bottom two subcells. Since 3JLM cells have been commercially available for some years, we use them as a reference design for comparative evaluation of the more novel 3JIMM and 4JLM designs.

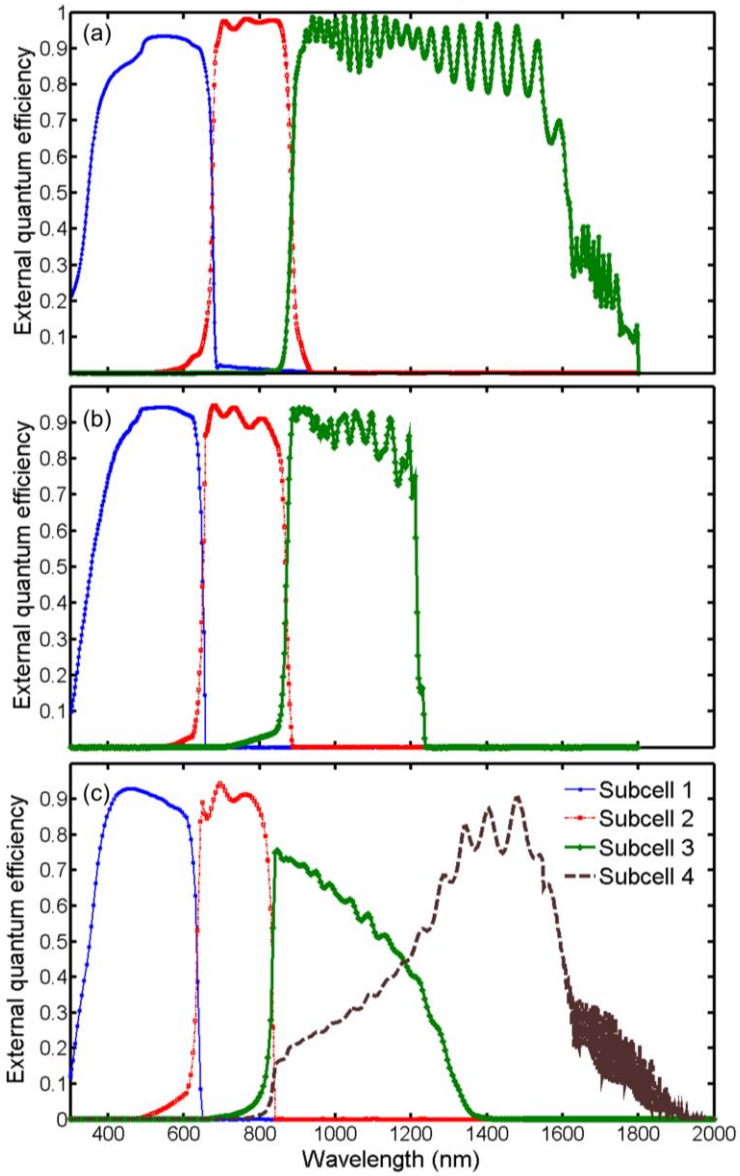

Fig. 2 External quantum efficiency as a function of wavelength for (a) the 3JLM (b) the 3JIMM and (c) the 4JLM solar cell. The significant differences in EQEs affect the optimal parameters for the optical system for each design.

Modeling is performed under standard test conditions (STC: 25ºC and 1000 W/m^2) with an ASTM G173-03 AM1.5D spectrum as the ray source. Distributed circuit models of each MJSC are developed by curve-fitting a parametrized, two-diode, equivalent circuit model to subcell *I-V* curves. These curves are generated by Sentaurus Device using the virtual contact method [25], under uniform illumination by the normalized spectrum of the smallest two-dimensional symmetry element of the MJSC. The width of this element is half that of the finger spacing, which ensures that lateral current flows are accurately determined while minimizing computational time [26].

2.2. Distributed circuit model

The distributed circuit consists of *n* functional blocks (see Fig. 10 in Appendix), determined from the number of grid lines; it effectively comprises a two-dimensional cross section of the MJSC,

transverse to the grid lines. The circuit is simulated using LTspice software by Linear Technology [27]. Since the subcell distributed circuit must see only those spectral components that it may harvest, we multiply the intensity-normalized AM1.5D spectrum by the subcell EQE to acquire a virtual spectrum [28]. The relative optical power in each subcell block is found by ray tracing the total power in its virtual spectrum through the optical train adjusted for grid line shading. Note that this is the integrated optical power across the entire subcell depth, parallel to the grid line. The local current source for each block is then determined by rescaling the Sentaurus-derived subcell short circuit current density by the functional block area, the relative optical power within that area, the 1000 W/m^2 reference intensity, and the geometric concentration.

System efficiency is determined for each MJSC from the *I-V* curve extracted from SPICE simulations of its distributed circuit. This is done across the range of critical system dimensions, and the maximum system efficiency is identified for each design under both uniform and nonuniform illumination conditions. Uniform illumination conditions are achieved by averaging each subcell irradiance profile over the entire subcell area. This will permit comparative assessment between MJSC designs for the spectral and spatial variations induced by their optimized systems.

2.3. Concentrating system optical design

The CPV system has an optical train comprising a primary optical element (POE) and a secondary optical element (SOE), for a geometric concentration of 1250X. Optical losses in the system lead to a 15-20% decrease in efficiency and, therefore, the MJSC receives ~1000X concentration. The POE is a Fresnel lens made of solar-grade polymethylmethacrylate (PMMA) [29] modeled as an idealized lens with no groove losses. The SOE is a truncated pyramid homogenizer modeled in BK7 glass. The system, shown in Fig. 3, is simulated by Monte-Carlo ray tracing using Zemax OpticStudio optical design software [30]. Material characteristics and the associated transmission, dispersion and reflection properties are included in the simulations. Scattering effects arising due to surface roughness have been neglected and so the simulations may represent a worst case scenario in terms of degree of nonuniformity since these effects tend to smooth out the irradiance peaks [28, 31].

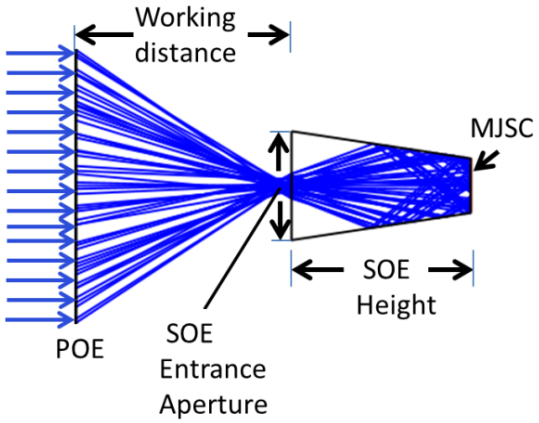

Fig. 3 Optimization parameters defined for the 2-stage optical system. Sunlight (from the left hand side) falls on the Fresnel POE and the rays are then incident on to the SOE entrance aperture with the focal point varying as function of the wavelength. The incident rays undergo total internal reflection, reflecting off the walls of the SOE, finally

reaching the MJSC at the exit aperture of the SOE via a lossless interface. Losses arising due to the height of the grid contacts are ignored in our simulation.

Fresnel lens parameters as used in Zemax are detailed in the Appendix (Table 5). Simulations are performed with 1 million rays for each spectrum (across 200 wavelengths) for a range of critical system dimensions. Fixing the POE parameters, these dimensions are the primary-to-secondary working distance, the SOE entrance aperture, and the SOE height, as detailed in Fig. 3.

We first consider the response of the optical system itself to gain insight into the nominal sensitivity of the illumination profile to variation in critical system dimensions. This permits us to more carefully choose the range of parameter space over which the full system efficiencies are to be calculated, so that actual system sensitivities to parameter variation can be assessed in the neighborhood of the maximum system efficiency.

The primary-to-secondary working distance determines if the lens focal point for a given wavelength is positioned inside or outside the SOE. It influences the number of total internal reflections in the SOE. Figure 4(a) shows the position of the focal point at a wavelength of 550 nm for POE-SOE working distances of (i) 250 mm and (ii) 260 mm using a fixed SOE height of 33 mm and an SOE entrance aperture of 20 mm. The two distances, 250 and 260 mm, are chosen in order to demonstrate the effect of the focal point being inside the SOE and outside the SOE and how that would affect ray paths. We choose a monochrome design initially for simplification and select the 550 nm wavelength for demonstration, since this wavelength lies within the top cell absorption range, which in typical MJSC designs, is the current limiting subcell. A loss in optical efficiency at this wavelength will imply a reduction in the number of photons reaching the top subcell, thereby limiting the overall system efficiency. A more detailed optical transfer function based analysis encompassing the entire wavelength range is performed in section 3.1 to demonstrate the effects of parametric variations.

Ray color change is used to visualize the number of internal reflections in a path. For the shorter working distance of 250 mm, the focal point lies inside the SOE and less internal reflections are found. For the longer distance, the focal point lies outside the SOE and the rays diverge before hitting the SOE, and homogeneity is improved, but at the cost of a 16% loss in optical efficiency due to the escaping rays. For the 260 mm distance, the rays are no longer confined to the SOE and the total internal reflection condition is not satisfied. The focal point of the Fresnel lens varies as a function of wavelength due to the dispersion in the PMMA, implying that the optimal working distance will be wavelength dependent. In the case of longer wavelengths, the focal length increases and the loss in optical efficiency may not occur at 260 mm but instead at working distances > 260 mm.

By increasing the height of the SOE (from 25 to 35 mm) for fixed working distance, we increase the number of total internal reflections in the SOE. An increase in total internal reflection implies an increase in spatial uniformity. Figure 4(b) shows ray-traces at a wavelength of 550 nm for two different SOE heights, (i) 25 and (ii) 35 mm, for a fixed working distance of 250 mm and an entrance aperture of 20 mm. At an SOE height of 25 mm, the peak-to-average irradiance ratio (PAR) is approximately 1.3; for the longer SOE (35 mm), the increased distribution of red and blue rays striking the MJSC indicates an increase in the number of multiple reflections, resulting in an improved homogeneity and a PAR = 1.1. The difference in optical efficiencies is negligible (~ 0.1%).

Increasing the width of the SOE entrance aperture increases the angle at which rays strike the SOE wall, leading to a loss of confinement when total internal reflection is no longer typically

satisfied; this reduces the optical efficiency. This is illustrated in Fig. 4(c) by comparison of ray traces at 550 nm for entrance apertures of (i) 16 and (ii) 40 mm, at a fixed working distance of 250 mm and a height of 33 mm. All the rays are contained within the SOE for the narrower width, but for the wider width, there is a marked failure to satisfy total internal reflection leading to a 50% reduction in optical efficiency. Optimal aperture widths vary based on concentration and optical design. Various types of SOE and corresponding aperture widths have been specified in [31] with SOE entrance to exit aperture width ratios varying from 1.5 to 2.5.

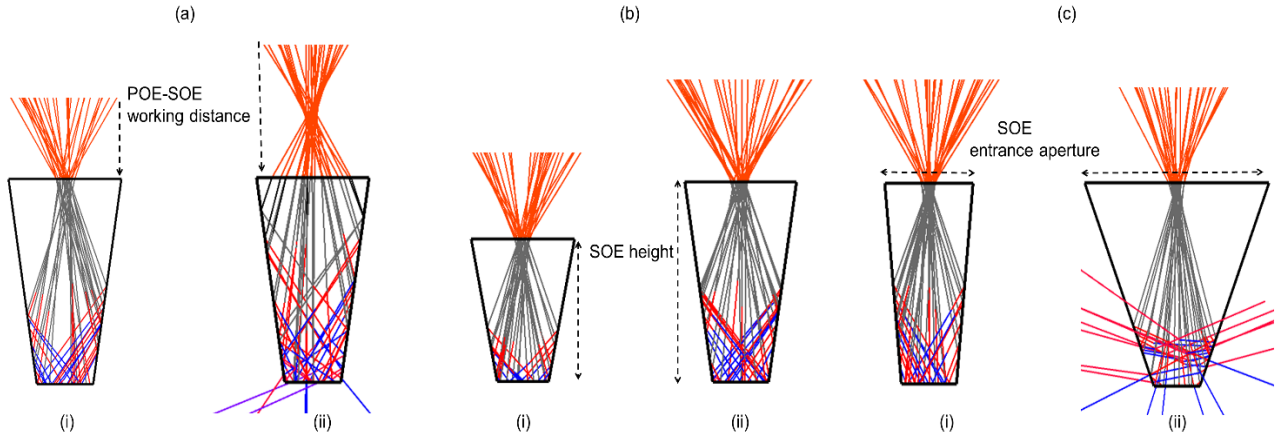

Fig. 4 Ray traces displaying the variation in the location of Fresnel lens focal point and the total internal reflection as a result of a change in (a) POE-SOE working distance (b) SOE height, and (c) the SOE entrance aperture width at a wavelength of 550 nm.

Ray tracing here can serve as a visual optimization tool to determine a range to narrow on an optimal value. The working distance was changed to 260 mm to demonstrate that any working distance other than the optimal can have a significant effect on the optical efficiency. A similar study was done to demonstrate that the change in SOE height and entrance aperture has a similar effect. The main objective of this demonstration was to show that these three parameters can significantly affect system efficiencies.

3. Results

3.1. Spectral variation with spatial uniformity

To first consider only the impact of spectral variation from the STC, we eliminate any spatial dependence in the optical transfer function (OTF) by calculating the average profile intensity for each wavelength. Figure 5(a) shows the dependence of the optical transfer function on wavelength for four different values of the POE-SOE working distance. The OTF, expressed as an optical efficiency, is determined for 161 wavelengths within a range from 360 to 2000 nm. The entrance aperture and the height of the SOE are fixed at 16 and 35 mm, respectively. At short wavelengths, the OTF rises more rapidly as the working distance decreases, with optical efficiencies plateauing at wavelengths > 500 nm. Little change in the OTF is seen over the rest of the spectrum, except at the shortest of working distances, where from about 1200 nm to 2000 nm a decrease of about 20%

is noted. This is mainly due to the escaping rays and a failure to satisfy total internal reflection within the SOE at longer wavelengths. Consequently, the top subcell should be the most sensitive to variations in the working distance. Figure 5(b) shows the dependence of the OTF on wavelength for four different values of the SOE height. The OTF is determined for a primary-to-secondary working distance of 250 mm and an entrance aperture width of 16 mm. Little change in optical efficiency is seen over most of the spectrum except around 400 nm for the shortest height (as shown in the inset). For SOE heights ranging from 20 to 40 mm, a small reduction in the OTF is seen at wavelengths above 1540 nm. One anticipates negligible impact on system efficiency for the three-junction designs since the 3JLM has an overproducing bottom subcell and the 3JIMM is spectrally unresponsive to wavelengths above 1400 nm. A modest impact, however, can be expected for the 4JLM design due to its broad absorption range and its current-matched bottom subcell. An optical efficiency reduction in the bottom subcell range of absorbed wavelengths would imply a current-limiting bottom subcell and a decrease in system efficiency.

Figure 5(c) shows the dependence of the OTF on wavelength for four different values of the SOE entrance aperture width. The OTF is determined for a primary-to-secondary working distance of 250 mm and an SOE height of 35 mm. A very strong dependence on aperture width is seen across all wavelengths, increasingly so for larger apertures, and especially towards wavelengths < 770 nm. This arises from a loss in total internal reflection. There will, therefore, be a marked impact on system efficiencies for all designs with any significant departure from the optimal SOE width.

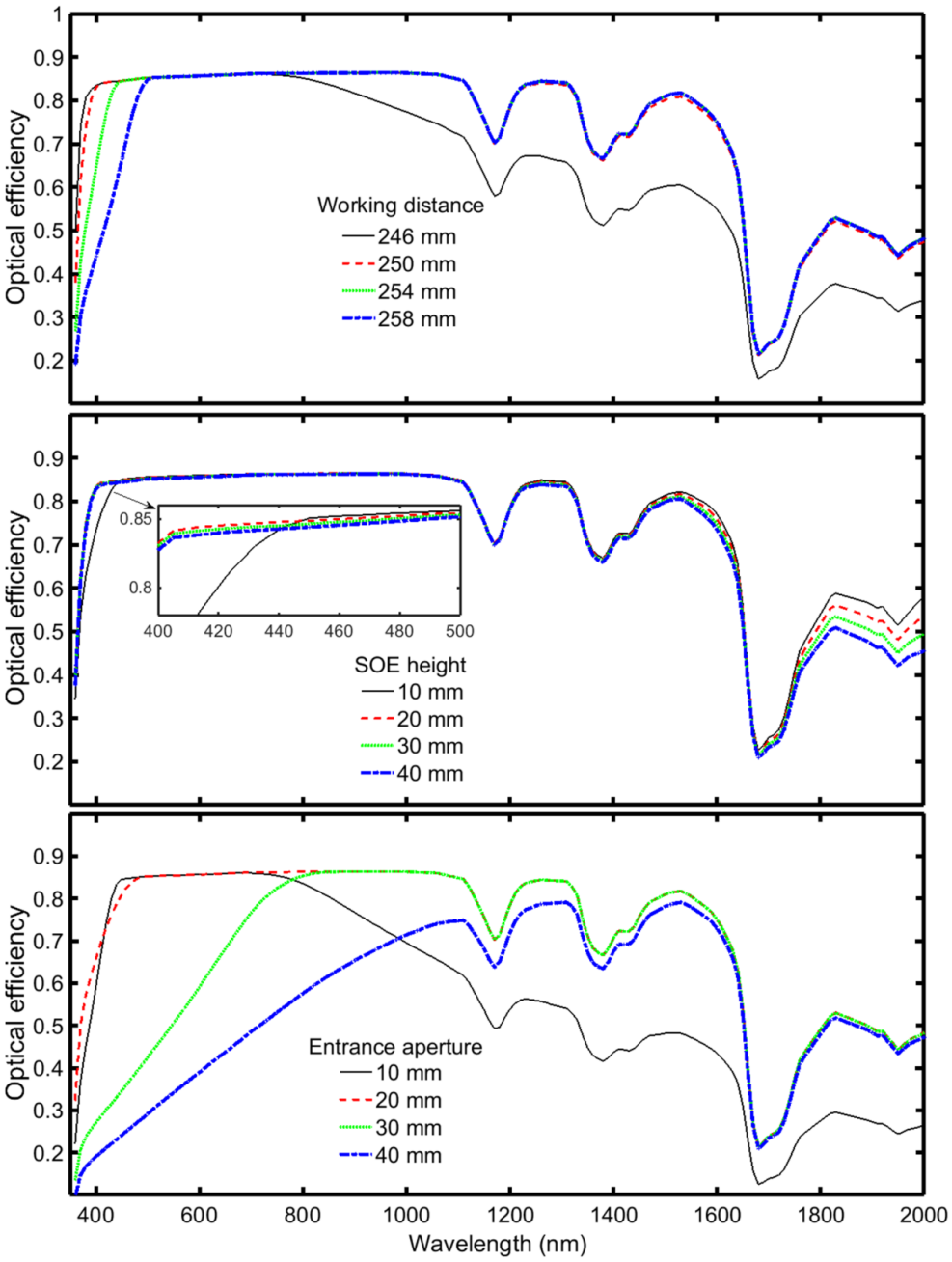

Fig. 5 Optical transfer function as a function of wavelength for different (a) POE-SOE distances (b) SOE heights, inset shows the variation in the optical transfer function between 400 and 500 nm, and (c) SOE entrance aperture widths.

We now determine full system efficiencies with each MJSC, as per our methodology, across the nominal parameter ranges for working distance, SOE height, and aperture width. To see system sensitivities to these parameters, we present the multidimensional results in Fig. 6 as system efficiency contour plots at the optimal entrance aperture width for each design. Each color bar peaks at its maximum system efficiency and spans a one percent (absolute) range, so that the three designs may be quantitatively compared. We note that all designs show a reasonably well-defined but broad "peak" about their system maximum. They all show comparable response to variations

in height, working distance, and aperture width of <0.02%, < 0.05%, and <0.3% (absolute) per mm, respectively, in the vicinity of their system efficiency maximum. The range of entrance aperture widths in Fig. 6 is only from 14-20 mm where as in Fig. 4 it is over a range 4 times the initial value. In addition, the effect of OTF on system efficiency is guided strongly by the EQE and the current-limiting subcell and therefore, a lower sensitivity to entrance aperture widths is seen in this analysis. While a larger working distance range (> 251 mm) was simulated for the 4JLM, in order to allow for simultaneous efficiency comparison with the other two designs, the plot has been limited to show the global maximum, which occurs at 251 mm. The efficiency drops if the working distance is increased further. The optimal parameter values are summarized in Table 1. Interpreting these values in light of the variations seen in Fig. 6 implies that one system design may be marginally suitable for all cell designs without suffering dramatic loss in efficiency. For example, using 3JIMM and 4JLM cells in a 3JLM optimized system gives absolute loss penalties of <0.1% and ~1%, respectively.

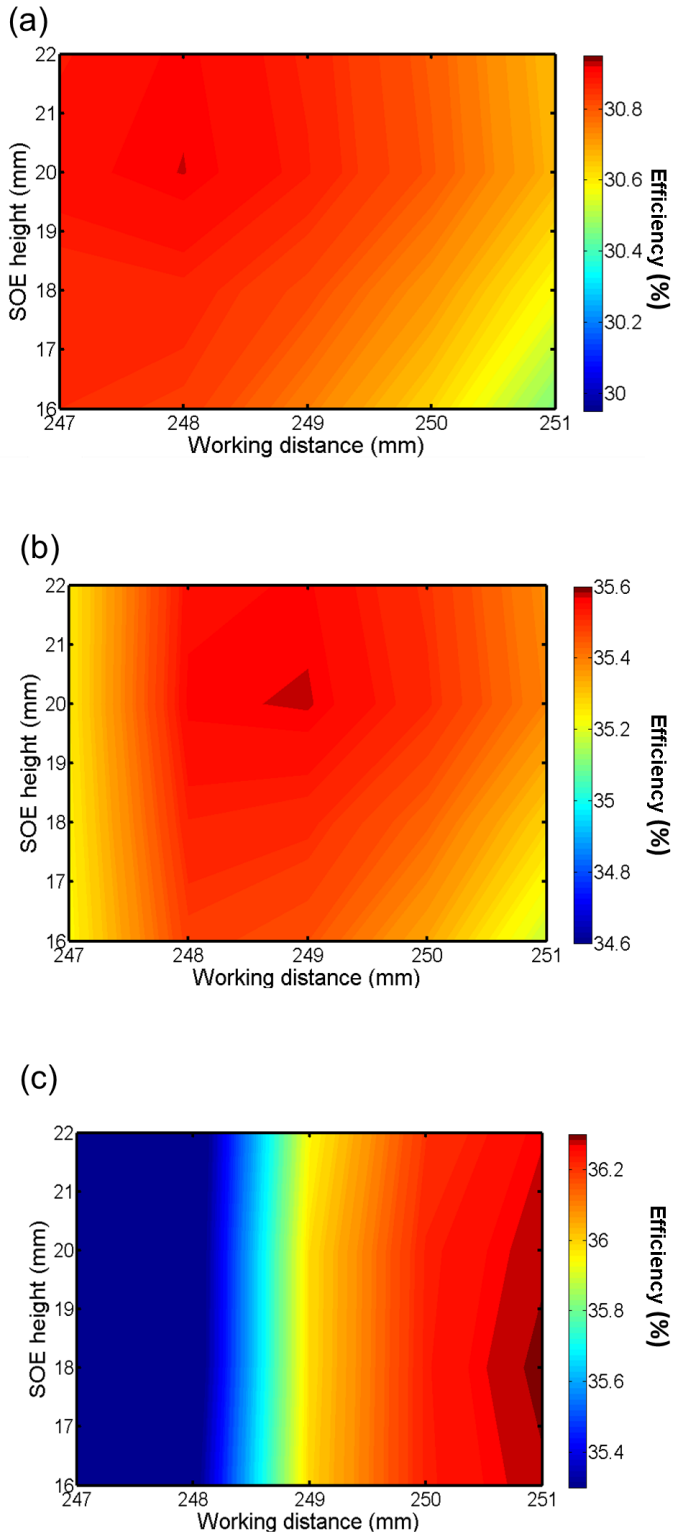

Fig. 6 Contour plots showing the maximum efficiency based only on spectral variation ignoring spatial effects for (a) 3JLM (b) 3JIMM and (c) 4JLM designs. The color bar shows the efficiency for each design. All plots have the same parameter ranges; the efficiency range is also fixed, at 1% absolute for each design. The efficiencies are shown at a fixed, optimal entrance aperture width (16 mm for all designs).

Table 1. Optimal parameter values (mm) for maximum system efficiency with a 10 mm SOE exit aperture.

Design	**Uniform illumination**			**Non-uniform illumination**		
	Working distance	*Entrance aperture*	*Height*	*Working distance*	*Entrance aperture*	*Height*
3JLM	248	16	20	249	16	37
3JIMM	249	16	20	251	16	36
4JLM	251	16	18	252	18	36

We summarize maximum system efficiencies and MJSC efficiencies in Table 2. Note that all efficiencies are for uniform illumination at 1250X, so that comparison extracts the loss penalty due to the OTF. A loss penalty may be associated with dispersive and non-dispersive components. We are interested in the former, since the spectral variations associated with dispersion may alter the current balance between subcells. The non-dispersive component is seen by inspection of the OTF plateaus to be 15% (between ~ 400 - 1100 nm) and does not alter current balance. The loss penalty is given as a relative (to the cell) percentage less this baseline to permit quantitative design comparison since the cells have different efficiencies. Clearly, however, the greatest improvement in system response would be achieved by decreasing this baseline loss, which is predominantly due to reflections at the various interfaces.

Table 2 shows that spectral variations impose loss penalties of lower than 2% for all three systems. The comparable loss penalties for the three-junction systems are primarily because the current balances between subcells one and two are disturbed by similar roll-offs on the blue end of their OTFs. The 3JIMM sees a slightly lower loss penalty than does the 3JLM because its bottom subcell does not see spectral variations in the OTF beyond 1200 nm, whereas the 3JLM does; that the difference is not larger is due to overproduction in the 3JLM bottom subcell. The larger loss penalty for the 4JLM system is primarily due to how the current balance between subcells one and four is impacted by the OTF; the fourth subcell sees a greater impact than the first, while subcells two and three are largely unaffected.

Table 2. Design efficiencies (absolute %) and corresponding loss penalties.

Design	**Maximum Efficiency (%)**			**Loss Penalty (Relative %)**		
	Cell (STC)	*Uniform illumination*	*Non-uniform illumination*	*Spectral variation only**	*Spectral + spatial variation**	*Spatial variation only*
3JLM	36.9	30.9	30.5	1.3	2.3	1.1
3JIMM	42.4	35.6	34.0	1.0	4.8	3.8
4JLM	43.5	36.3	35.3	1.6	3.9	2.3

* A non-dispersive baseline of 15% has been subtracted to show the effect of the variation.

3.2. Spectral and Spatial variations

In the previous section, the spatial variation in spectral mismatch has been neglected. To provide more realistic system efficiency estimates, we used in our fully-two-dimensional distributed circuit model, the actual illumination profiles generated by ray tracing. Again, full system efficiencies were determined using within nominal ranges around system efficiency maxima. The results are shown in Fig. 7 as contour plots at the optimal entrance aperture width. The color bars now span a three percent (absolute) range, in contrast to the one percent span in our earlier analysis. In contrast to earlier, all designs show a sharp "peak" about the system maximum. The three-junction designs show similar responses to variations in height, of about 0.3% (absolute) per mm, while the four-junction design has sensitivities of 0.8% and 0.1% per mm for heights lower and higher than optimal, respectively. The three-junction designs show a 0.6% per mm design sensitivity in working distance while the four-junction design has a 1.5% per mm sensitivity. For the entrance aperture width, the sensitivities for all designs are <0.3% per mm.

The optimal parameter values are again summarized in Table 1. Comparison with the uniform illumination case finds similar values for working distances and entrance apertures, but dramatically different values for SOE heights. The now almost doubled SOE heights are required to enable total internal reflection to homogenize the nonuniform profile as much as possible. Comparison also reveals system efficiencies now far more sensitive to variations in working distance and SOE height, greater than ten times both for the height and the working distance. The sensitivity to entrance aperture width stays less than 0.3% per mm. Interpreting parameter values in light of the variations seen in Fig. 7 implies that one system design cannot be used for all cell designs without suffering a dramatic loss in efficiency. For example, using 3JIMM and 4JLM cells in a 3JLM optimized system gives absolute loss penalties of 1 and 3.4%, respectively. This is in marked contrast to the earlier case; it underlines the critical need for a full system optimization under realistic cell illumination conditions.

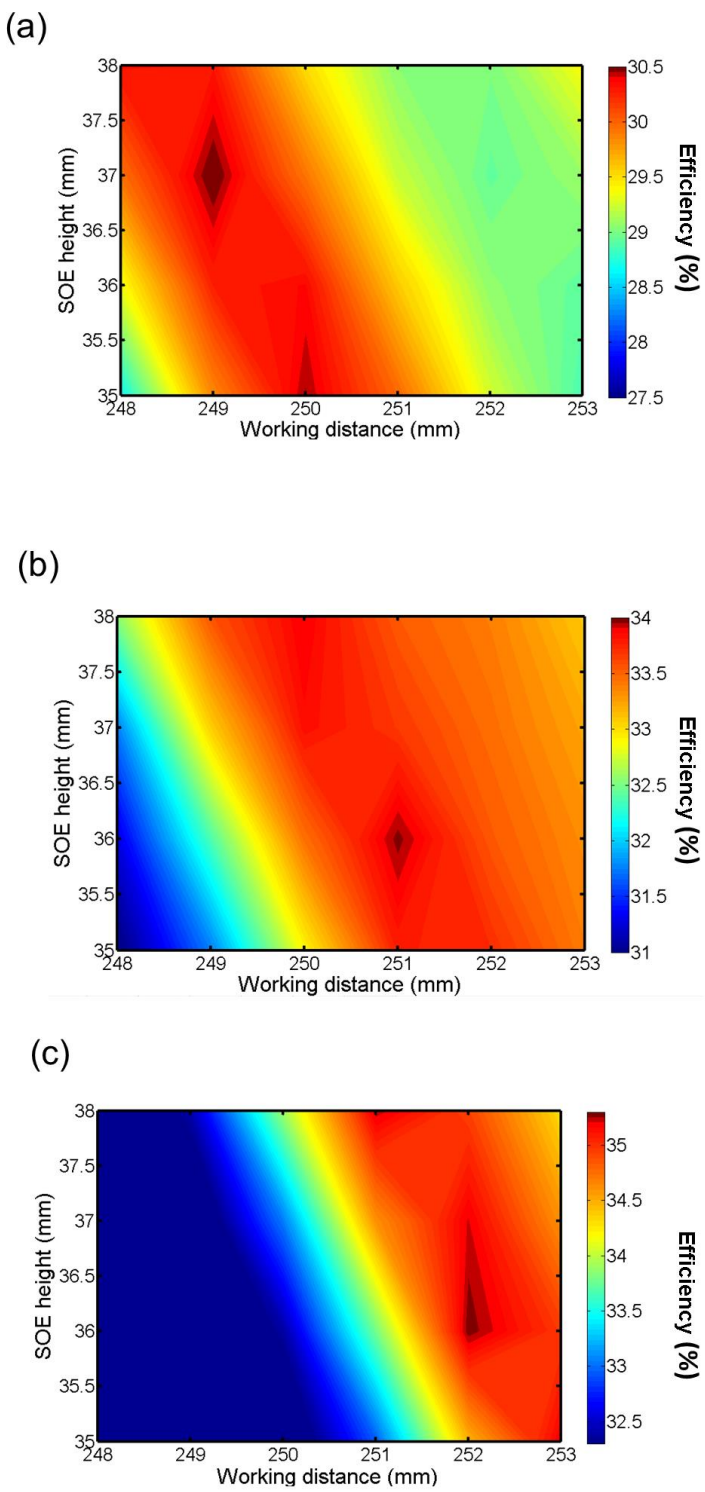

Fig. 7 Contour plots showing the maximum efficiency including both spatial and spectral variations for (a) 3JLM (b) 3JIMM and (c) 4JLM designs. The efficiencies are shown at a fixed, optimal entrance aperture width (16 mm for 3JLM and 3JIMM designs and 18 mm for 4JLM designs). The color bars now span over a 3% absolute range for system efficiency. The contour plot for the 3JLM design shows a global maximum as well as a local maximum. A wide range of parameter values has been studied to obtain a global maximum.

We again summarize maximum system efficiencies in Table 2. Comparison of results obtained under uniform and nonuniform illumination reveals that maximum efficiencies under nonuniform illumination are systematically lower than under uniform illumination: the most marked reduction is for the IMM design, while the impact appears to worsen for the LM designs as the number of junctions increase. To ascertain the origin of such losses, we again quantify in Table 2 the system loss relative to its cell by a loss penalty. The impact of both spectral and spatial variations on the 3JIMM design is seen to be more than twice as severe as their impact on the 3JLM design (4.8% vs. 2.3%); their impact on the 4JLM design lies between these values. To gain further insight, we assume spatial and spectral effects can linearly decouple and so subtract the "spectral only" loss penalty from the "spectral + spatial" loss penalty to determine the loss penalty due solely to spatial variations. We assume that lateral resistances do not significantly impede current low and so there is an instantaneous lateral flow of charge. This allows for automatic current balancing between the functional units. Therefore, it is valid to linearly decouple spatial and spectral variations.

Loss penalty due to spatial variations is more than 3.5 times greater for the 3JIMM design (3.8%) than for the 3JLM design (1.1%), but only about twice as great for the 4JLM design (2.3%). The impact of spatial variation on the 3JIMM design is seen to be a much more severe than the impact of spectral variation, somewhat more severe for the 4JLM design, and slightly less severe for the 3JLM design. To understand these dependencies, we need to consider the current distributions within each subcell. For each design, Fig. 8 shows the distributed circuit source currents, which are calculated from the subcell short-circuit current distributions as described in section 2.3. For the 3JLM design, Figure 8(a) shows that the top subcell clearly limits current production across the entire device. The middle subcell slightly overproduces in the central region, but is otherwise well matched; the bottom subcell heavily overproduces at the edges, and is only well matched in a smaller central region. The small loss penalty of 1.1% noted in Table 2 is therefore likely due to minor lateral current flows associated with matched currents that are slightly higher (by about 20%) in the central region than on the edges.

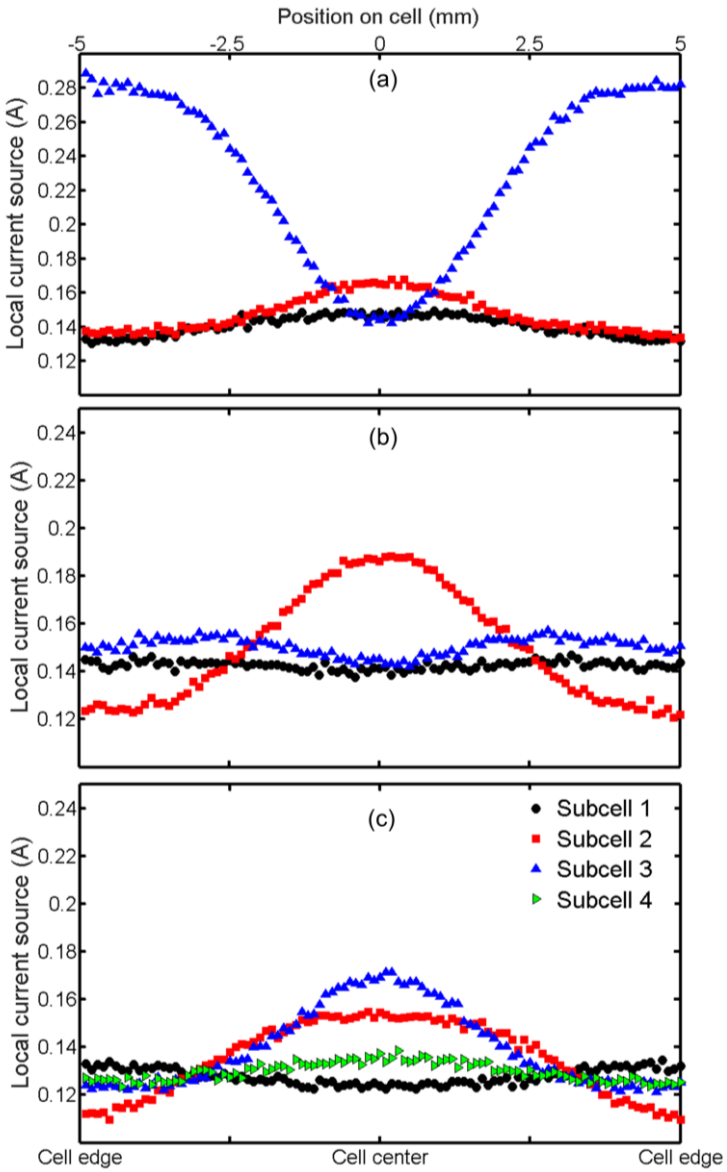

Fig. 8 Local current source distributions on the (a) 3JLM (b) 3JIMM and (c) 4JLM cells at the optimal parameter values as obtained using our full system optimization. The local current source value is obtained by rescaling the current density obtained at 1000 W/m^2, the illuminated area within a functional unit, the relative optical power within that area, and the geometric concentration. Bottom subcell limiting behavior cannot be ignored for fully current-matched configurations, such as the 3JIMM and the 4JLM in our study.

For the 3JIMM design, Fig. 8(b) shows top and bottom subcells closely current matched across their reasonably flat profiles. However, the middle subcell strongly overproduces in the central region, but correspondingly underproduces at the edges. All else being equal, lateral current flows in the middle cell from the center to the edge should act to achieve an overall current balance, yielding negligible loss penalty. The large loss penalty of 3.8% noted in Table 2 arises from the dissipative effect of the large lateral resistances (on average, ~6.9 Ω– see Table 3 in the Appendix) and higher overall currents. The same is true to a lesser degree for the 4JLM design, where subcell currents shown in Fig. 8(c) have distributions similar to that of the 3JIMM cell. Again, top and bottom subcells are closely current matched across their reasonably flat profiles. The middle two

subcells strongly overproduce in the central region, but only subcell 2 significantly underproduces at the edges. Lower peak-to-average irradiance ratios, and less dissipation, due to somewhat smaller subcell 2 lateral resistances (on average, ~2.4 Ω – see Table 4 in Appendix) and lower overall currents, means a smaller spatial loss penalty should be observed, as is indeed noted in Table 2.

In order to further investigate the sensitivity of the 3JIMM design to spatially nonuniform illumination profiles, we simulate the 3JIMM with the middle cell receiving nonuniform, Gaussian illumination, while the top and bottom subcells receive uniform illumination under 1250 suns. With an aim to simulate varying optical effects, different Gaussian peak-to-average values have been used. We vary the lateral resistance of the middle subcell (R_{sc2}) and determine the relative increase in efficiency. Fig. 9 shows the relative efficiency increase under various Gaussian profiles with lateral resistances reduced by 3/4, 1/2, 1/4th of the initial sheet resistance value.

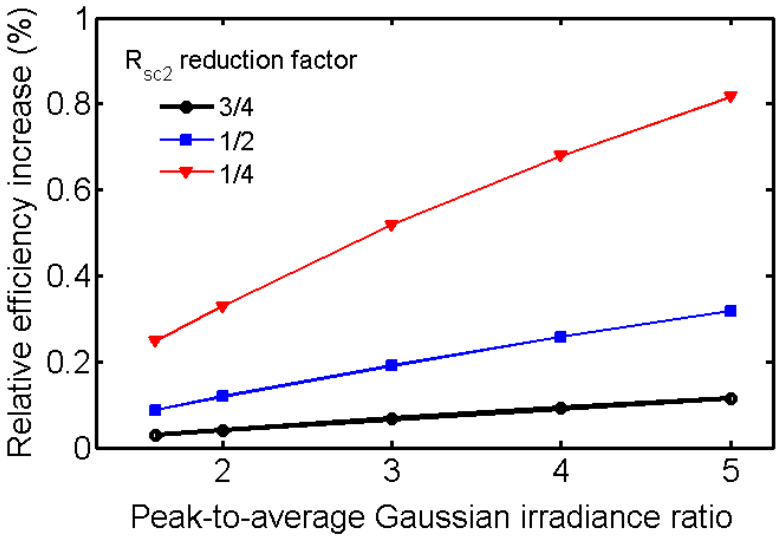

Fig. 9 Relative efficiency increase as a function of the peak-to-average Gaussian irradiance ratio for the 3JIMM design, with varying lateral resistance of the middle subcell. The top and the bottom subcells receive uniform illumination.

This analysis allows us to determine the impact of high lateral resistances on the efficiency of the TJIMM, specifically under highly nonuniform profiles (PAR= 5) and provides a means to mitigate losses due to spatially nonuniform illumination. It can be seen that a non-negligible (> 0.2% relative) increase in efficiency can be observed if the lateral resistance is reduced to 1/4 of the original value, even for the profile with a PAR =1.6. The efficiency increase is more pronounced for higher PARs, implying that the detrimental effect of highly nonuniform profiles can be partly mitigated by reducing subcell lateral resistances, allowing for current spreading. A similar result has been reported in [9] for a 3JLM cell.

4. Conclusions

Multiparameter system optimization using integrated opto-electrical modeling, employing ray tracing and SPICE modeling, is carried out for 3JLM, 3JIMM and 4JLM cell designs. A consequence of the optical system are the nonuniform spatial and spectral illumination profiles at the MJSC with loss penalties varying, depending on the MJSC design. Nonuniform illumination, although represents a less-than-ideal scenario for MJSCs, its effect can be partly mitigated by

allowing excessive currents to flow laterally through alternative paths. However, high lateral resistances impede current flow and cause loss penalties. While spectral variations alone have the greatest impact (<1.5% relative loss penalty) on the 4JLM design due to its longer wavelength absorption range, loss penalties due to spatial variations are significantly higher (<3.5% relative) for 3JIMM design, primarily due to its high lateral resistance. Lateral resistance varies depending on layer thicknesses, doping concentrations and mobilities of charge carriers. These parameters are typically optimized for maximum efficiency under uniform illumination profiles, leading to loss penalties under realistic, nonuniform illumination profiles. Such loss penalties may be reduced if the MJSC subcell layers are specifically designed to accommodate nonuniform illumination profiles generated by optics. Our results also indicate that optical system optimization be performed in concert with the specific MJSC design in order to obtain maximum system efficiencies.

Acknowledgments

We would like to thank Alex Walker and Anna Trojnar for performing the numerical modeling of the 3J designs. We acknowledge the support from the National Science and Engineering Research Council of Canada, the Canadian Foundation for Innovation, Canada Research Chair Program and Ontario Research Fund. We gratefully acknowledge CMC Microsystems for providing access to Sentaurus and Zemax software.

Appendix

A1. MJSC layer structures

Table 3 shows the layer structure, along with material details, thicknesses and doping concentrations for the three MJSC designs.

Table 3 Layer structures for (a) 3JLM (b) 3JIMM and (c) 4JLM designs

(a) 3JLM layer structure

Layer Name	Material composition	Thickness (µm)	Doping Concentration (cm^{-3})
Subcell 1 front surface field	n-$Al_{0.5}In_{0.5}P$	0.03	1.00E+19
Subcell 1 emitter	n-$Ga_{0.5}In_{0.5}P$	0.1	5.00E+18
Subcell 1 base	p-$Ga_{0.5}In_{0.5}P$	0.75	1.00E+17
Subcell 1 back surface field	p-$(Al_{0.25}Ga_{0.75})_{0.5}In_{0.5}P$	0.12	1.00E+18
Tunnel junction (p-type)	p-$Al_{0.15}Ga_{0.85}As$	0.02	6.00E+19
Tunnel junction (n-type)	n-$Al_{0.15}Ga_{0.85}As$	0.02	3.00E+19
Subcell 2 front surface field	n-$Ga_{0.5}In_{0.5}P$	0.03	5.00E+18
Subcell 2 emitter	n-$In_{0.01}Ga_{0.99}As$	0.08	1.00E+18
Subcell 2 base	p-$In_{0.01}Ga_{0.99}As$	3.5	1.00E+17
Subcell 2 back surface field	p-$Ga_{0.5}In_{0.5}P$	0.1	1.00E+19
Tunnel junction (p-type)	p-$Al_{0.3}Ga_{0.7}As$	0.05	4.00E+20
Tunnel junction (n-type)	n-GaAs	0.05	2.00E+19
Subcell 3 buffer	n-$In_{0.01}Ga_{0.99}As$	0.2	2.00E+18
Subcell 3 front surface field	n-$Ga_{0.5}In_{0.5}P$	0.02	5.00E+19
Subcell 3 emitter	n-Ge	0.1	1.00E+19

Subcell 3 base	p-Ge	170	2.00E+17

(b) 3JIMM layer structure

Layer Name	Material composition	Thickness (μm)	Doping Concentration (cm^{-3})
Subcell 1 front surface field	n-$Al_{0.5}In_{0.5}P$	0.05	1.00E+19
Subcell 1 emitter	n-$Ga_{0.5}In_{0.5}P$	0.04	2.00E+18
Subcell 1 intrinsic region	p-$Ga_{0.5}In_{0.5}P$	0.3	1.00E+16
Subcell 1 base	p-$Ga_{0.5}In_{0.5}P$	0.41	1.00E+17
Subcell 1 back surface field	p-$(Al_{0.25}Ga_{0.75})_{0.5}In_{0.5}P$	0.1	1.00E+18
Tunnel junction (p-type)	p-$Al_{0.3}Ga_{0.7}As$	0.03	2.00E+19
Tunnel junction (n-type)	n-$Al_{0.3}Ga_{0.7}As$	0.03	2.00E+19
Subcell 2 front surface field	n-$Ga_{0.5}In_{0.5}P$	0.03	5.00E+18
Subcell 2 emitter	n-$ln_{0.01}Ga_{0.99}As$	0.07	3.00E+18
Subcell 2 intrinsic region	p-$ln_{0.01}Ga_{0.99}As$	0.5	5.00E+15
Subcell 2 base	p-$ln_{0.01}Ga_{0.99}As$	1.8	1.00E+17
Subcell 2 back surface field	p-$Ga_{0.5}In_{0.5}P$	0.1	1.00E+19
Tunnel junction (p-type)	p-$Al_{0.3}Ga_{0.7}As$	0.03	2.00E+19
Tunnel junction (n-type)	n-GaAs	0.03	2.00E+19
Subcell 3 buffer	n-$Ga_{0.99}In_{0.01}As$	0.2	1.00E+18
Subcell 3 buffer	n-$Ga_{0.51}In_{0.49}P$	0.25	5.00E+15
Subcell 3 buffer	n-$Ga_{0.47}In_{0.53}P$	0.25	5.00E+15
Subcell 3 buffer	n-$Ga_{0.43}In_{0.57}P$	0.25	5.00E+15
Subcell 3 buffer	n-$Ga_{0.39}In_{0.61}P$	0.25	5.00E+15
Subcell 3 buffer	n-$Ga_{0.35}In_{0.65}P$	0.25	5.00E+15
Subcell 3 buffer	n-$Ga_{0.31}In_{0.69}P$	0.25	5.00E+15
Subcell 3 buffer	n-$Ga_{0.27}In_{0.73}P$	0.25	5.00E+15
Subcell 3 buffer	n-$Ga_{0.22}In_{0.78}P$	1	5.00E+15
Subcell 3 buffer	n-$Ga_{0.25}In_{0.75}P$	0.25	5.00E+15
Subcell 3 emitter	n-$Ga_{0.7}In_{0.3}As$	0.1	1.00E+18
Subcell 3 base	p-$Ga_{0.7}In_{0.3}As$	4	1.00E+16

(c) 4JLM layer structure

Layer Name	Material composition	Thickness (μm)	Doping Concentration (cm^{-3})
Subcell 1 front surface field	n-$Al_{0.5}In_{0.5}P$	0.025	6.00E+18
Subcell 1 emitter	n-$Ga_{0.5}In_{0.5}P$	0.1	5.00E+18
Subcell 1 base	p-$Ga_{0.5}In_{0.5}P$	0.65	8.00E+16
Subcell 1 back surface field	p-$Al_{0.5}In_{0.5}P$	0.05	3.00E+19

Tunnel junction (p-type)	p-$Al_{0.3}Ga_{0.7}As$	0.03	2.00E+20
Tunnel junction (n-type)	n-$Ga_{0.5}In_{0.5}P$	0.03	6.00E+19
Subcell 2 front surface field	n-$Al_{0.79}Ga_{0.2}In_{0.01}$ As	0.03	1.00E+19
Subcell 2 emitter	n-$Al_{0.05}Ga_{0.94}$ $In_{0.01}As$	0.1	3.00E+18
Subcell 2 base	p- $Al_{0.05}Ga_{0.94}$ $In_{0.01}As$	2	1.00E+17
Subcell 2 back surface field	p-$Al_{0.4}Ga_{0.59}$ $In_{0.01}As$	0.08	1.00E+19
Tunnel junction (p-type)	p-$Al_{0.3}Ga_{0.69}$ $In_{0.01}As$	0.03	1.20E+20
Tunnel junction (n-type)	n-$Al_{0.05}Ga_{0.94}$ $In_{0.01}As$	0.03	6.00E+19
Subcell 3 front surface field	n- $Ga_{0.99}$ In $_{0.01}As$	0.05	1.00E+19
Subcell 3 intrinsic region	n-$In_{0.11}Ga_{0.89}AsN$*	0.65	2.00E+15
Subcell 3 back surface field	p- $Ga_{0.99}$ In $_{0.01}As$	0.05	1.00E+19
Tunnel junction (p-type)	p-$Al_{0.3}Ga_{0.69}$ $In_{0.01}As$	0.03	1.20E+20
Tunnel junction (n-type)	n-$Ga_{0.99}$ In $_{0.01}As$	0.03	6.00E+19
Subcell 4 front surface field	n-Ga $_{0.99}$ $In_{0.01}As$	0.05	7.00E+17
Subcell 4 emitter	n-Ge	0.1	5.00E+18
Subcell 4 base	p-Ge	170	1.00E+18

* The InGaAsN subcell is effectively InGaAs with 11% In, 89% Ga, which is then diluted with 3.7% Nitrogen.

A2. Distributed circuit model details

Figure 10 shows a single functional unit of the distributed circuit model of a four-junction design with an illuminated and shaded unit, similar to the model of a three-junction design described in [8]. This functional unit is a fraction of the area and is repeated *n* times to simulate the entire cell area. The efficiency of the cell is calculated for the entire cell area. Lateral resistances, R_L, connect cells across the rows in the model and are obtained from the sheet resistance values for each layer. Series resistance in a solar cell is dominated by the electrode resistance, which can vary significantly with the choice of the design. Since all the cells have the same number of contacts and equal finger widths, the effect of electrode resistance would be additive to the lateral resistance. The variation in lateral resistance between the designs is more pronounced, and so in order to see the effects of lateral resistance, we have set the electrode resistance (R_{se}) to be negligible. The electrode resistance, however, is a variable parameter in the model and can be customized to any value.

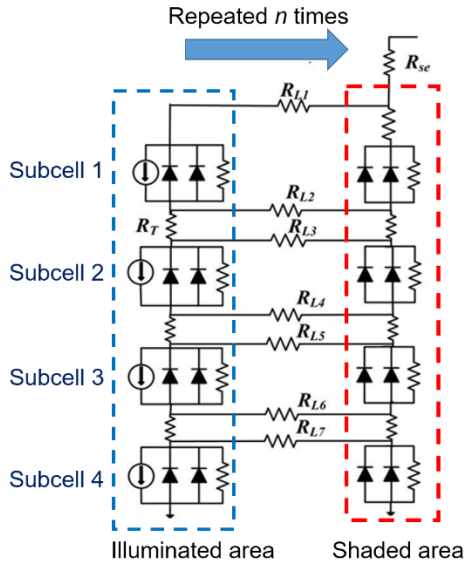

Fig. 10 Single functional unit of a four-junction solar cell in the distributed circuit model. Lateral current flow is inhibited by the lateral resistances (R_L) calculated from the sheet resistances of the individual layers.

The SPICE parameters used for the MJSC designs are detailed in Table 4. The values are fitted on the basis of the two diode equation as follows:

$$I = I_L - I_{01}\left\{exp\left[\frac{q(V+IR_S)}{kT}\right]-1\right\} - I_{02}\left\{exp\left[\frac{q(V+IR_S)}{2kT}\right]-1\right\} - \frac{V+IR_S}{R_{sh}} \quad (1)$$

where I_L is the light-generated current (which is directly proportional to the solar irradiation), I_{01} and I_{02} are reverse saturation currents, q is the electronic charge, k is Boltzmann constant, R_S is the series resistance, R_{sh} is the shunt resistance, V is the output voltage and I is the output current of the solar cell.

The values for the circuit parameters and the lateral resistance, R_L , as used in the distributed model is listed in Table 3.The sheet resistance of the 3JIMM top subcell is adjusted to determine the lateral resistance to fit to the *I-V* curves of the Sentaurus model at various concentrations. In the case of the 3JLM and 3JIMM designs, the middle cell open circuit voltages are 0.88 and 1.04 V respectively, hence the difference in the recombination current values.

Table 4 The SPICE parameters for the three MJSC designs as used in the distributed circuit model.

3JLM	I_{01} **(A)**	I_{02} **(A)**	R_{sh} **(kΩ)**	R_L **(Ω)**
Top subcell	5.5×10^{-26}	4.3×10^{-15}	4.0	R_{L1} = 1.1 R_{L2} = 27.0
Middle subcell	2.0×10^{-17}	1.5×10^{-10}	4.0	R_{L3} = 1.1 R_{L4} = 2.7
Bottom subcell	1.4×10^{-6}	2.2×10^{-5}	4.6	R_{L5} = 0.2
3JIMM				
Top subcell	3.0×10^{-27}	2.5×10^{-14}	4.0	R_{L1} = 2.2 R_{L2} = 42.1

Middle subcell	4.3 x10^{-20}	8.7 x10^{-12}	3.0	R_{L3} = 0.6 R_{L4} = 13.2
Bottom subcell	3.7 x10^{-11}	2.1 x10^{-7}	2.0	R_{L5} = 1.3
4JLM				
Top subcell	7.1 x 10^{-29}	4.0 x10^{-16}	6.0	R_{L1} = 1.3 R_{L2} = 7.6
Middle subcells	3.0 x10^{-20} 2.2 x10^{-8}	1.0 x10^{-12} 6.0 x10^{-5}	3.4 7.3	R_{L3} = 0.6 R_{L4} = 4.2 R_{L5} = 0.4 R_{L6} = 6.3
Bottom subcell	3.5 x10^{-7}	2.9 x10^{-12}	1.0	R_{L7} = 0.4

A3. Fresnel lens parameters

The Fresnel lens profile used for our CPV system is entered in the ray tracing software using the following general sag equation used for a typical aspheric lens [32]:

$$z(r) = \frac{cr^2}{1+\sqrt{1-(1+k)c^2r^2}} + \alpha_1 r^2 + \alpha_2 r^4 + \cdots + \alpha_8 r^{16} \quad (2)$$

Here, c represents the base curvature at vertex, k is the conic constant, r is radius from optic axis and $\alpha_i r^{2i}$ are the higher order aspheric terms. The groove losses and scattering effects are ignored for our simulations. The Fresnel lens parameters entered in the ray trace are shown in Table 5.

Table 5 Fresnel lens parameters as used in ray tracing models.

Parameter	Value
Conic constant (k)	-1
α_1	1.0 x 10^{-4}
α_2	6.8x10^{-9}
α_3	-3.3x10^{-14}
Radial Height	177 mm
Half width	177 mm
Thickness	2.3 mm
Radius (r)	127.5 mm

These parameters were obtained by using Zemax's in-built optimization tool. The starting Fresnel lens parameters were obtained from a commercially available Fresnel lens manufacturer [33] and further optimized (within 50 optimization cycle limit) for maximum optical efficiency under AM15D spectrum at this concentration.

Acknowledgement

We would like to thank the National Science and Engineering Research Council of Canada, the Canadian Foundation for Innovation, Canada Research Chair program, and Ontario Research Fund for supporting this work and CMC Microsystems for providing licenses for Sentaurus and Zemax software.

References

[1] Press Release. Fraunhofer Institute for solar energy systems, 1 December 2014. URL: https://www.ise.fraunhofer.de/en/press-and-media/press-releases/press-releases-2014/new-world-record-for-solar-cell-efficiency-at-46-percent (last accessed on September 7, 2016).

[2] Technical Report. 2015. “Current status of concentrator photovoltaic technology,” NREL and Fraunhofer ISE.

[3] Baig, Hasan, Keith C. Heasman, and Tapas K. Mallick. 2012. “Non-Uniform Illumination in Concentrating Solar Cells.” Renewable and Sustainable Energy Reviews 16 (8): 5890–5909 [doi:10.1016/j.rser.2012.06.020].

[4] Franklin, E., and J. Coventry. "Effects of highly non-uniform illumination distribution on electrical performance of solar cells." In: ANZSES Solar Conference, Newcastle, Australia (2002).

[5] Gordon, Jeffrey M., Eugene A. Katz, Wondesen Tassew, and Daniel Feuermann. 2005. “Photovoltaic Hysteresis and Its Ramifications for Concentrator Solar Cell Design and Diagnostics.” Applied Physics Letters 86 (7): 73508 [doi:10.1063/1.1862776].

[6] Mellor, A., J. L. Domenech-Garret, D. Chemisana, and J.I. Rosell. 2009. “A Two-Dimensional Finite Element Model of Front Surface Current Flow in Cells under Non-Uniform, Concentrated Illumination.” Solar Energy 83 (9): 1459–65 [doi:10.1016/j.solener.2009.03.016].

[7] Domenech-Garret, Juan-Luis. "Cell behaviour under different non-uniform temperature and radiation combined profiles using a two dimensional finite element model." Solar Energy 85, no. 2 (2011): 256-264.

[8] Sharma, Pratibha, Alex W. Walker, Jeffrey F. Wheeldon, Karin Hinzer, and Henry Schriemer. 2014. “Enhanced Efficiencies for High-Concentration, Multijunction PV Systems by Optimizing Grid Spacing under Nonuniform Illumination.” International Journal of Photoenergy 2014: 1–7. [doi:10.1155/2014/582083].

[9] García, Iván, Pilar Espinet-González, Ignacio Rey-Stolle, and Carlos Algora. 2011. “Analysis of Chromatic Aberration Effects in Triple-Junction Solar Cells Using Advanced Distributed Models.” IEEE Journal of Photovoltaics 1 (2): 219–24 [doi:10.1109/JPHOTOV.2011.2171671].

[10] Ota, Yasuyuki, and Kensuke Nishioka. 2012. “Three-Dimensional Simulating of Concentrator Photovoltaic Modules Using Ray Trace and Equivalent Circuit Simulators.” Solar Energy 86 (1): 476–81 [doi:10.1016/j.solener.2011.10.021].

[11] Domínguez, César, Ignacio Antón, Gabriel Sala, and Stephen Askins. 2013. “Current-Matching Estimation for Multijunction Cells within a CPV Module by Means of Component Cells: Current-

Matching Estimation for MJ Cells within a Concentrator." Progress in Photovoltaics: Research and Applications 21 (7): 1478–88 [doi:10.1002/pip.2227].

[12] Cotal, H., and R. Sherif. 2005. "The Effects of Chromatic Aberration on the Performance of GaInP/GaAs/Ge Concentrator Solar Cells from Fresnel Optics." In , 747–50. IEEE [doi:10.1109/PVSC.2005.1488240].

[13] Nishioka, Kensuke, Tatsuya Takamoto, Takaaki Agui, Minoru Kaneiwa, Yukiharu Uraoka, and Takashi Fuyuki. 2004. "Evaluation of InGaP/InGaAs/Ge Triple-Junction Solar Cell under Concentrated Light by Simulation Program with Integrated Circuit Emphasis." Japanese Journal of Applied Physics 43 (3): 882–89 [doi:10.1143/JJAP.43.882].

[14] Galiana, B, C Algora, and I Reystolle. 2006. "Comparison of 1D and 3D Analysis of the Front Contact Influence on GaAs Concentrator Solar Cell Performance." Solar Energy Materials and Solar Cells 90 (16): 2589–2604 [doi:10.1016/j.solmat.2006.02.013]

[15] Espinet-González, Pilar, Ignacio Rey-Stolle, Carlos Algora, and Ivan Garcia. 2015. "Analysis of the Behavior of Multijunction Solar Cells under High Irradiance Gaussian Light Profiles Showing Chromatic Aberration with Emphasis on Tunnel Junction Performance." Progress in Photovoltaics: Research and Applications 23 (6): 743–753.

[16] Sharma, Pratibha, Matthew Wilkins, Henry Schriemer, and Karin Hinzer. 2014. "Modeling Nonuniform Irradiance and Chromatic Aberration Effects in a Four Junction Solar Cell Using SPICE." In, 3293–97. IEEE [doi:10.1109/PVSC.2014.6925639].

[17] Sharma, Pratibha, Alex Walker, Jeff Wheeldon, Henry Schriemer, and Karin Hinzer. 2013. "Optimization of Finger Spacing for Concentrator Photovoltaic Cells under Non-Uniform Illumination Using SPICE." In Photonics North 2013, 891505–891505. International Society for Optics and Photonics.

[18] TCAD Sentaurus by Synopsys, Mountainview, USA.
URL: http://www.synopsys.com/Tools/TCAD/ProcessSimulation/Pages/SentaurusProcess.aspx (last accessed: June 17, 2016).

[19] Walker, Alex W., Olivier Thériault, Matthew M. Wilkins, Jeffrey F. Wheeldon, and Karin Hinzer. 2013. "Tunnel-Junction-Limited Multijunction Solar Cell Performance over Concentration." IEEE Journal of Selected Topics in Quantum Electronics 19 (5): 1–8.

[20] Walker, A. W., O. Thériault, and K. Hinzer. 2014. "Carrier Dynamics in Quantum-Dot Multijunction Solar Cells under Concentration." IEEE Journal of Photovoltaics 4 (4): 1095–99 [doi:10.1109/JPHOTOV.2014.2322279].

[21] Geisz J.F., et al. "High-efficiency GaInP/GaAs/InGaAs triple-junction solar cells grown inverted with a metamorphic bottom junction," Applied Physics Letters 91, 023502, 2007.

[22] Wilkins, Matthew M., Ahmed Gabr, Pratibha Sharma, Henry Schriemer, and K. Hinzer. 2014. "4-Junction Solar Cells with Dilute Nitrides: Optimization with Luminescent Coupling," In European Photovoltaic Solar Energy Conference, Amsterdam, The Netherlands.

[23] Arbez, G. et al., "4 Junction Dilute Nitride Solar Cell Optimization: Comparing Current Matching Approaches in Detailed Balance Algorithms," 39th IEEE Photovoltaic Specialists Conference, 2013.

[24] Wheeldon, J. F., Valdivia, C. E., Walker, A. W., Kolhatkar, G., Jaouad, A., Turala, A., Riel, B., Masson, D., Puetz, N., Fafard, S., Arès, R., Aimez, V., Hall, T. J. and Hinzer, K. 2011, "Performance comparison of AlGaAs, GaAs and InGaP tunnel junctions for concentrated multijunction solar cells." Progress in Photovoltaics: Research and Applications 19: 442–452.

[25] Walker, A.W. (2013), "Bandgap engineering of multijunction solar cells using nanostructures for enhanced performance under concentrated illumination."
URL:
https://www.ruor.uottawa.ca/bitstream/10393/26240/3/Walker_Alexandre_William_2013_Thesis.pdf (last accessed: September 9, 2016).

[26] Philipps, Simon P., Wolfgang Guter, Elke Welser, Jan Schöne, Marc Steiner, Frank Dimroth, and Andreas W. Bett. 2012. "Present Status in the Development of III–V Multi-Junction Solar Cells." In Next Generation of Photovoltaics, 1–21.

[27] LTspice by Linear Technology, Milipitas, USA.
URL: http://www.linear.com/designtools/software/

[28] Victoria, M., R. Herrero, C. Domínguez, I. Antón, S. Askins, and G. Sala. 2013. "Characterization of the Spatial Distribution of Irradiance and Spectrum in Concentrating Photovoltaic Systems and Their Effect on Multi-Junction Solar Cells: Spatial Distribution: Irradiance and Spectrum." Progress in Photovoltaics: Research and Applications 21 (3): 308–18 [doi:10.1002/pip.1183].

[29] URL: http://www.acrylite-shop.com/pdfs/232-23-ACRYLITE-Solar-0Z023-en-Cyro.pdf (last accessed: Jan. 22, 2016).

[30] Zemax OpticStudio, Kirkland, USA.
URL: http://www.zemax.com/ (last accessed: June 17, 2016).

[31] Victoria, Marta, César Domínguez, Ignacio Antón, and Gabriel Sala. 2009. "Comparative Analysis of Different Secondary Optical Elements for Aspheric Primary Lenses." Optics Express 17 (8): 6487–6492.

[32] Spencer, G. H., and MVRK Murty. 1962. "General Ray-Tracing Procedure." JOSA 52 (6): 672–676.
[33] URL: http://www.fresneltech.com/pdf/FresnelLenses.pdf (last accessed: September 9, 2016).
.